



HAL
open science

Thermal characterization of polyethylene glycol 600 in liquid, solid phases and through the phase transition

Justine Noel, Yves Jannot, Christel Métivier, Nicolò R Sgreva

► **To cite this version:**

Justine Noel, Yves Jannot, Christel Métivier, Nicolò R Sgreva. Thermal characterization of polyethylene glycol 600 in liquid, solid phases and through the phase transition. *Thermochimica Acta*, 2022, 716, pp.179326. 10.1016/j.tca.2022.179326 . hal-03516867v5

HAL Id: hal-03516867

<https://hal.science/hal-03516867v5>

Submitted on 29 Sep 2022

HAL is a multi-disciplinary open access archive for the deposit and dissemination of scientific research documents, whether they are published or not. The documents may come from teaching and research institutions in France or abroad, or from public or private research centers.

L'archive ouverte pluridisciplinaire **HAL**, est destinée au dépôt et à la diffusion de documents scientifiques de niveau recherche, publiés ou non, émanant des établissements d'enseignement et de recherche français ou étrangers, des laboratoires publics ou privés.

Thermal characterization of polyethylene glycol 600 in liquid and solid phase and across the phase transition

Justine Noel^a, Yves Jannot^a, Christel Métivier^{a,*}, Nicolò R. Sgreva^a

^a*Université de Lorraine, LEMTA, CNRS, 54000 Nancy, France.*

Abstract

The polyethylene glycol (PEG) is characterized by experimental means in both solid and liquid phase. Main thermal properties inherent to the phase transition are also provided. More specifically, we focus on PEG 600, whose average molar mass is 600 g mol^{-1} and melting temperature transition is around 283-298 K. The phase change does not occur at a given temperature but rather over a range of temperature, highlighting the complexity of the material. Several methodologies have been developed and calibrated in order to obtain, in both phases, the density and the thermal conductivity. A temperature dependence fit is proposed for the density in liquid phase. The relative density variation from the liquid to solid phase is significant as it can reach about 35 %, meaning a quite large volume shrinkage. Differential Scanning Calorimetry (DSC) has been used for measuring the heat capacity of solid and liquid phase and the effective heat capacity at the transition states. The latent heat of fusion and solidification converge to a value of around 128 kJ kg^{-1} . Undercooling effects are mitigated by performing DSC with slow temperature variation rates. Lastly, we have also observed several exothermic peaks during the solidification process that are related to structural reorganizations of the material.

1. Introduction

2 Polyethylene glycol (PEG) is a polyether present in our daily life and its
3 employment covers a wide range of industries, such as cosmetics, pharma-
4 ceuticals, food manufacturing, inks. As an example, it is used as a thickener

*christel.metivier@univ-lorraine.fr

5 agent in cosmetic products (liquid soaps, moisturizers, shampoos, etc.) and
6 paramedical products (hydro-alcoholic gels, intimate lubricants [1], etc.). It
7 is also used as a solvent in printer inks or to manufacture paint balls, as a
8 food additive and in certain polyester resins. Because it is a bio-compatible
9 product [2], it is also widely used in medical treatments and vaccines [3], as
10 recently for Covid-19 vaccine. In addition, the polyethylene glycol presents
11 remarkable properties: from a chemical viewpoint it is stable, non corro-
12 sive and non toxic. Another significant advantage lies in the large variety
13 of temperatures at which the solid/liquid transition occurs. Depending on
14 PEG's molecular weight, phase transition occurs for instance around 283-
15 293 K for PEG 600, 321-323 K for PEG 1000 [4] and around 324 K for PEG
16 1500 [5]. For these reasons, numerous studies have been devoted to propose
17 Composite Phase Change Materials (CPCMs) based on polyethylene glycol
18 [6, 7, 8, 9, 10, 11, 12]. Phase change materials (PCMs) are widely studied
19 in the field of energy storage/release since a large amount of energy can be
20 transferred during the phase change via latent heat. Energy is stored during
21 endothermic transformations (e.g. solid to liquid) while it is released dur-
22 ing exothermic transformations. The large latent heat of PEG makes it a
23 very interesting and attractive PCM. Furthermore, it matches perfectly the
24 criteria related to the choice of PCMs, such as being low-cost, non-toxic,
25 non-flammable, non-corrosive and biodegradable (bio-compatible), i.e. eco-
26 friendly. The uses of PEG in Composite PCMs can concern thermal reg-
27 ulation in buildings [13] or pavements [8] as well as in photovoltaic panels
28 [4, 12].

29 Despite the wide use of PEG, only few papers were devoted to characterize
30 the thermal properties of polyethylene glycol alone. Recently, Kou et al. [14]
31 have measured heat capacities of PEG for molar mass varying from 2000 to
32 20 000 g mol⁻¹. For smaller molar mass, as it is the case of PEG 600 (average
33 molar mass of 600 g mol⁻¹), available data correspond mainly to properties
34 for the liquid phase only. For instance, density measurements are provided
35 by several authors [15, 16, 17, 18], but they are given only for the liquid phase
36 for few temperature values, not sufficient to obtain the thermal expansion
37 coefficient. Some properties of PEG 600 are also given by Lane [19] who
38 focuses on properties of several PCMs. For PEG 600, the author indicates
39 the latent heat of melting and only one value for the melting temperature.
40 Lane [19] also provides the thermal conductivity and the density in liquid
41 phase for a couple of temperature values. Only a few other studies present
42 the thermal conductivity of liquid phase, e.g. [17, 19]. Thus, properties of

43 PEG remain partially and scatteredly described in the literature. Moreover,
44 this small number of measured properties is obtained only for the liquid
45 phase. To our knowledge, the latent heat of solidification, the freezing point,
46 the thermal conductivity, the density and the heat capacity for the solid
47 phase are not available in the literature.

48 From a structural viewpoint, PEG's properties - in particular at the
49 solid/liquid transition - depend not only on the molecular weight but also
50 on the protocols involved in measuring them. Several types of aggregate
51 structures, such as helical or spherical conformations have been observed
52 within the freezing process [20, 21]. Understanding the correlation between
53 structural modifications and imposed experimental conditions is crucial since
54 the structural organization can have a significant impact on the macroscopic
55 properties. Indeed, in the case of semi-crystalline polymers as it is for PEG,
56 Bogdanov et al. [22] highlighted the influence of the cooling rate on the
57 exothermic crystallization peak by means of isothermal Differential Scan-
58 ning Calorimetry (DSC). Furthermore, a correlation between the heat flux
59 measured by DSC and the degree of crystallinity of PEG is proposed by
60 Pielichowski & Flejtuch [23].

61 As a first step in the understanding of the relationships between PEG's
62 behaviour and conditions of use, we clarify and provide new macroscopic
63 properties for PEG 600. The aim of our study is to characterize this polyether
64 in both the solid and liquid phase. In the liquid phase, we provide original
65 values of macroscopic properties and how they vary with temperature. In the
66 solid phase, we aim to fill the data gap in the literature. We carefully detail
67 the methodologies and protocols used to obtain the main thermal properties
68 in each phase (density, effective heat capacity and thermal conductivity) and
69 the latent heat of melting and solidification. In section 2, the different mea-
70 surement techniques and protocols used are detailed. Results are provided
71 in section 3 where they are also compared with the available literature. The
72 paper ends with conclusions and perspectives.

73 **2. Methods and experimental devices**

74 *2.1. Material*

75 Polyethylene glycol (PEG) is a linear polyether made from ethylene gly-
76 col monomers characterized by a molar mass generally smaller than 20 000
77 g mol^{-1} . In this study, we aim to characterize the polyethylene glycol with

78 molar mass of around 600 g mol^{-1} , named PEG 600 (Table 1). The sam-
79 ples of PEG 600 that we used were purchased in synthesis grade from Merck
80 (CAS 25322-68-3, labeled average molecular mass of $570\text{-}630 \text{ g mol}^{-1}$) and
81 were used as received, i.e. without further purification. Several batches have
82 been used to verify reproducibility of results (batches numbers: S8111586
83 136 and S8111586 121).

84 The temperature of the solid-liquid phase change is indicated by the sup-
85 plier within the range of $290.15\text{-}293.15 \text{ K}$.

86 The initial degree of purity of the material is not stated in the product
87 specifications provided by the manufacturer and has not been subsequently
88 measured. However, [18] report an initial purity of $\geq 99.8\%$ for PEG 600
89 provided by the same manufacturer as our (same CAS number). No purifi-
90 cation method was used in [18]. For this reason, and considering the good
91 agreement we have obtained in thermophysical properties with available lit-
92 erature (see next section 3), no further purification was performed on our
93 PEG samples.

94 The water content (w) in our samples is estimated by taking the weight
95 of PEG samples before and after drying them at 353.15 K for 24 hours (see
96 supplementary materials). We have found a water content of 0.24% , with a
97 combined expanded uncertainty $U_c(w) = 0.02 \%$ with 0.95 level of confidence
98 (coverage factor $k=2$).

99 In Table 1 we also report the samples of water, glycerol and sapphire em-
100 ployed during methods validation. We used ultra-pure water (Anton Paar)
101 to verify density measurements obtained with the densimeter. We used glyc-
102 erol for the validation of the transient hot needle method used to estimate
103 thermal conductivity. For the validation of other analysis methods we used
104 demineralized water. The latter is produced by a reverse osmosis unit from
105 Ondeo (Purite Select A640/GP, $1\text{-}10 \text{ M}\Omega \text{ cm}$). To ensure good water quality,
106 filter cartridges are changed before the water resistance drops to $1 \text{ M}\Omega \text{ cm}$.
107 We underline that the water resistance is given directly by the device when it
108 is produced. Finally, a sapphire sample was used to validate the solid phase
109 heat capacity measurements (see also Section 2.4 of this article and Section
110 2.3 of the supplementary material). The sample corresponds to a cylinder of
111 5 mm height, 2.5 mm diameter and 97.0 mg mass.

112

Table 1: Samples table

Chemical Name	Source	Initial Mass Fraction Purity, x_e	Purification Method ^a
Polyethylene	Merck	-	none
Glycol 600	CAS 25322-68-3	-	none
Ultra-pure water	Anton Paar	-	none
Demineralized water	Tap water	-	reverse osmosis
Glycerol	Fisher Chemical CAS 56-81-5	0.99	none
Sapphire (solid cylinder)	Setaram	-	none

^afurther purification in addition to that of the supplier ('Source')

113 *2.2. Density*

114 *2.2.1. Liquid phase*

115 The density (ρ) of PEG 600 in liquid phase is measured by using a den-
 116 simeter DMA 5000M, Anton Paar. The densimeter provides a 10^{-6} g cm $^{-3}$
 117 accuracy in the temperature range of 273.15-333.15 K, while for larger tem-
 118 peratures (up to a maximum of 373.15 K) the accuracy decreases to 10^{-4}
 119 g cm $^{-3}$. The precision on the temperature is 0.01 K. Calibration and valida-
 120 tion of the device are given in the supplementary material. Density measure-
 121 ments are carried out at constant pressure P (atmospheric pressure) and at
 122 different temperature values within the range of 294.15-373.15 K where PEG
 123 600 is liquid. Isothermal conditions are obtained by imposing temperature
 124 steps with a 1 K increment in the range 294.15-323.15 K, followed by a 5 K
 125 increment up to the temperature of 373.15 K. In the liquid phase, the time
 126 to achieve the thermal stability is about 5 minutes per temperature step.

127 To ensure reproducible results, density is measured on three different
 128 samples (volume of ~ 1 mL) from two different batches. At a given temper-
 129 ature, the maximal variation between measurements is found to be 2×10^{-5}
 130 g cm $^{-3}$. The final value of density is taken as the mean of these measure-
 131 ments. From the temperature dependence of the density, we evaluate the
 132 thermal expansion coefficient β as follows

$$\beta = -\frac{1}{\rho_{ref}} \left(\frac{\partial \rho}{\partial T} \right)_P, \quad (1)$$

133 with $\rho_{ref} = \rho(T_{ref})$ being a reference density defined at the temperature T_{ref} .
 134 The thermal expansion coefficient indicates the first-order density variations

Table 2: Pressure measurements performed for the pycnometer calibration at 273.75 K - Steps (1) and (2). P_i is the initial pressure and P_f the final pressure ^a.

Step (1)			Step (2)		
P_i (bar)	P_f (bar)	P_f/P_i	P_i (bar)	P_f (bar)	P_f/P_i
3.654	1.685	46.1 %	3.655	2.002	54.7 %
3.660	1.696	46.3 %	3.650	2.002	54.8 %
3.665	1.706	46.5 %	3.603	1.976	54.8 %

^aStandard uncertainties u are $u(P) = 0.001$ bar and $u(T) = 0.01$ K.

135 with temperature (Boussinesq approximation) at constant pressure [24] and,
 136 for a given mass of a material, it also corresponds to the volume variation
 137 with temperature.

138 2.2.2. Solid phase

139 The density of PEG 600 in solid phase is achieved using a lab-made
 140 pycnometer. The device is placed in a thermostatic enclosure BinderTM
 141 KBF 115 in order to control the temperature. The temperature set in the
 142 binder is 273.75 K in order to ensure that our PEG sample will be fully
 143 solid. The pycnometer consists in two different cavities of volume V and V'
 144 separated by a valve, as represented in Fig. 1. The measurement procedure
 145 is to initially obtain the vacuum in both cavities, i.e. $P' = P = 0$, then close
 146 the valve and impose a pressure P_i to the lower cavity. The valve is then
 147 opened involving pressure variations until an equilibrium is reached within
 148 the two cavities, leading to a final pressure P_f . The pressure is measured
 149 using a Mano 2000 Leo 3 Keller with an accuracy of 1 mbar.

150 We first start by a calibration of the device, i.e. we determine the volumes
 151 V and V' of each cavity by repeating several times the above mentioned
 152 procedure through Steps (1) and (2), as indicated in Fig. 1 b. Volumes V
 153 and V' are determined via the following equation

$$P_i V = P_f \times (V + V' - V_{ref}), \quad (2)$$

154 where V_{ref} corresponds to the volume of a cylinder of height 0.02 m and
 155 radius 0.04 m. The procedure is repeated three times. Measurements are
 156 summarized in Table 2. The precision of the method has been evaluated by
 157 performing step (3) using a calibrated volume of solid. Details are provided
 158 in the supplementary material.

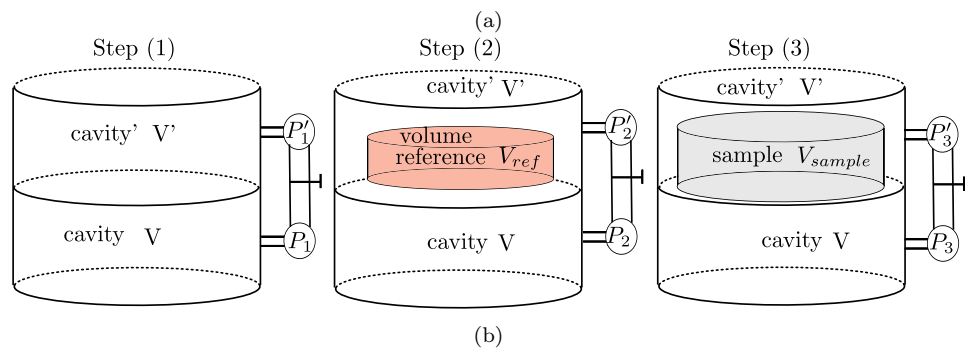


Figure 1: (a) Photo of the pycnometer. (b) Sketch of the set-up for calibration - Step (1) and Step (2) - and for measuring the density of solid PEG 600 - Step (3) -.

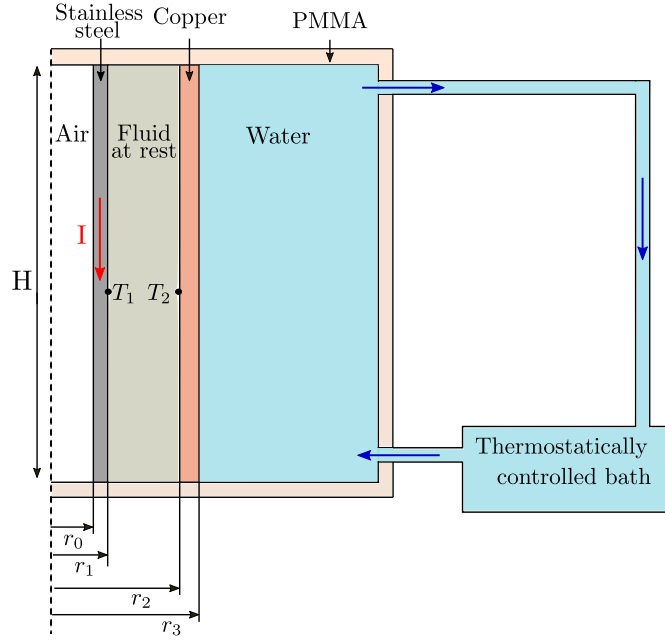


Figure 2: Sketch of the hot tube device used for thermal conductivity measurements. $r_0 = 2.54$ mm, $r_1 = 2.75$ mm, $r_2 = 6.00$ mm

159 Finally, Step (3) is performed with a given mass of PEG (Fig. 1 b). The
 160 volume of solid PEG is obtained using eq. (2) in which V_{ref} is replaced by
 161 the unknown sample volume. The density of PEG in solid phase is deduced
 162 from this measurement.

163 2.3. Thermal conductivity

164 2.3.1. Liquid phase

The thermal conductivity of the liquid phase is measured via the stationary hot tube method [25, 26]. A sketch of the device developed in our laboratory is shown in Fig. 2. A validation of the device with demineralized water is provided in the supplementary material. The sample is introduced in liquid phase into the gap between two coaxial cylinders made of copper (the outer one) and stainless steel (the inner one). We ensure that the sample fills completely the space between the two cylinders, i.e. the space between r_1 and r_2 in Fig. 2. An electric current I is applied to the inner cylinder, producing heat flux by Joule effect. The outer part of the copper cylinder is maintained at a given temperature via a temperature controlled water flow. The temperatures T_1 and T_2 are measured using two type K thermocouples

locked on the wall of the cylinders, i.e. at the boundaries of the liquid layer (as indicated in Fig. 2). Moreover, in order to avoid any up-down wall effects, thermocouples are located at the mid-height of the device. The temperature difference is measured thanks to the voltage difference U between these two thermocouples:

$$\Delta T = T_1 - T_2 = U/k,$$

165 where k is a constant equal to $k = (39.2 + 0.064 \times T_2 - 0.005 \times T_2^2) \times 10^{-6}$
 166 V K^{-1} . Thermocouples are connected to a cold junction block. Tension and
 167 electrical current are measured with a Keysight U3401A and an ISO-TECH
 168 IDM91E multimeter, respectively.

169 For a purely conductive regime in the liquid layer (fluid at rest), the
 170 thermal conductivity can be deduced as follows [25]:

$$\lambda = \frac{\rho_{el} I^2 \ln(r_2/r_1)}{2\pi^2(r_1^2 - r_0^2)\Delta T} \quad (3)$$

171 with $\rho_{el} = 7.3 \times 10^{-7}(1 + 1.36 \times 10^{-2}(T - T_{ref})) \Omega \text{m}$ being the electrical
 172 resistivity of the stainless steel and T_{ref} a temperature reference equal to
 173 293.15 K.

174 The dimensions of the device are determined under the condition that no
 175 convection occurs for a wide range of fluids. According to [27], we ensure
 176 that the following condition is satisfied:

$$\frac{Ra}{H^+} < 400 \quad (4)$$

177 where $H^+ = H/\delta$, H is the height of the cylinders, $\delta = r_2 - r_1$ is the thickness
 178 of the liquid layer and Ra corresponds to the Rayleigh number given by

$$Ra = \frac{\rho g \beta \Delta T \delta^3}{\mu a}, \quad (5)$$

179 with μ being the dynamic viscosity and a the thermal diffusivity of the
 180 fluid.

181 This condition is verified a posteriori and in the case of our measurements
 182 with PEG we estimate $Ra/H^+ \approx 15 - 20 \ll 400$.

183 Device validation performed with demineralized water leads to a maximal
 184 difference in thermal conductivity of 2.5 % with values provided by Ramires
 185 et al. [28], i.e. a variation of $0.02 \text{ W m}^{-1} \text{ K}^{-1}$ (see supplementary material).

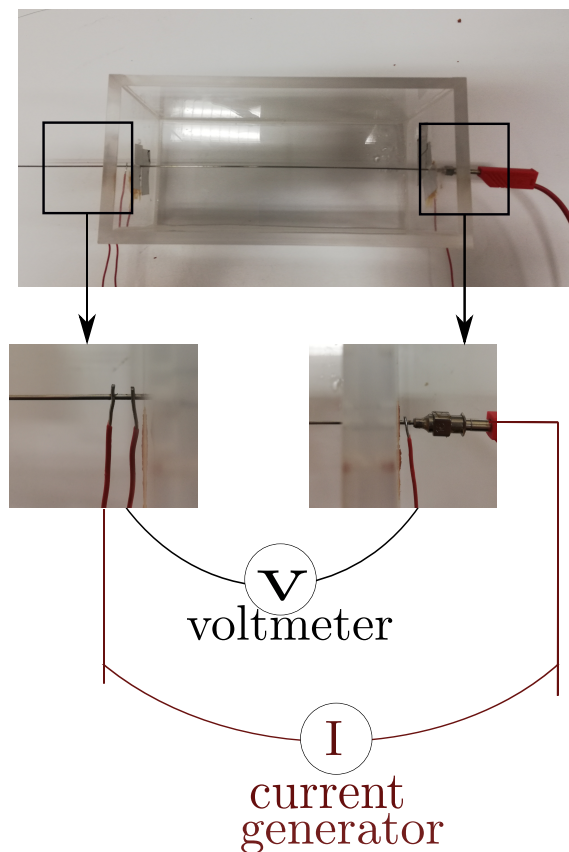


Figure 3: Photo of the heated needle device

186 Since the device is filled by the PCM in liquid phase, the volume of the sample
 187 varies with the temperature with a maximal variation occurring during the
 188 phase transition. As it is with most materials, PEG decreases in volume from
 189 liquid to solid phase. This can lead to imperfect contacts at walls during the
 190 solidification, as detailed in Appendix A. In this case, i.e. when thermal
 191 contact resistances are present at walls, the device becomes unsuitable for
 192 measuring thermal conductivity of materials in solid phase. For this reason,
 193 we propose another technique to carry out measurements in the solid phase.
 194 This technique is detailed in the following paragraph.

195 *2.3.2. Hot needle method*

196 We developed a specific device in order to measure the thermal con-
 197 ductivity of materials in solid or liquid phase. The device consists in a

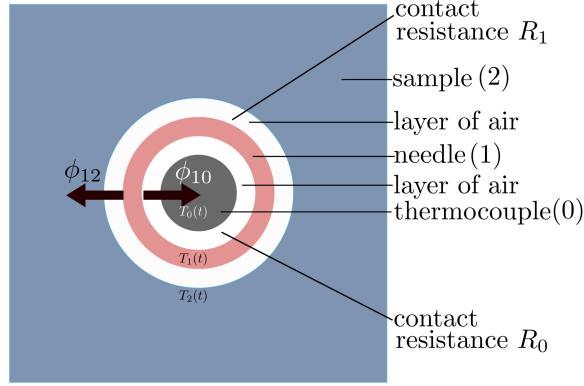


Figure 4: Schematic cross section of the hollow needle probe. The subscripts “0”, “1” and “2” refer to the thermocouple, the needle and the sample, respectively.

198 $200 \times 120 \times 120 \text{ mm}^3$ cavity made of PMMA that is filled with the sample.

199 A stainless steel hollow needle of length 300 mm is placed at the center
 200 of the device (Fig. 3). Needle’s inner and outer radii are $r_i = 0.80 \text{ mm}$ and
 201 $r_e = 1.25 \text{ mm}$, respectively. The needle is heated by Joule effect and the
 202 corresponding heat flow rate per unit of length L is $\phi = (UI)/L$, with U the
 203 electrical tension and I the electric intensity. Temperature is measured at the
 204 central point inside the needle with a K-type sheath thermocouple of radius
 205 $r_t = 0.5 \text{ mm}$. Electrical tension and current are measured with a Tektronix
 206 DMM and an ISO-TECH IDM91E multimeter, respectively. Temperatures
 207 are recorded using a TC-08 Picolog device with a frequency of 10 Hz.

208 According to Fig. 4, in the following description we use the subscripts
 209 “0”, “1” and “2” to refer to the thermocouple, the needle and the sample,
 210 respectively.

211 The device is placed in a BinderTM KBF 115 thermostatic chamber in
 212 order to maintain the system at a controlled temperature. The thermostatic
 213 chamber also guarantee a constant initial temperature $T(t = 0)$ in the whole
 214 system, i.e. $T_0(0) = T_1(0) = T_2(0)$, being the initial temperature of the
 215 thermocouple, the needle and the sample, respectively. We assume uniform
 216 temperature field in the needle, $T_1(t)$, and in the thermocouple, $T_0(t)$, since
 217 they are very thin. Moreover, since contacts at interface 1-2, i.e. needle-
 218 sample, and at the interface 1-0, i.e. needle-thermocouple, are not perfect,
 219 also the thermal contact resistances R_1 and R_0 (see Fig. 4) have to be taken
 220 into account. Finally, due to the long length of the cavity, we consider an
 221 unidirectional dependence of parameters at the center of the cavity.

222 As the needle is heated, the total heat flow rate ϕ due to Joule effect can
 223 be split in two components, i.e. $\phi = \phi_{10} + \phi_{12}$ where ϕ_{12} is the heat transferred
 224 to the material and ϕ_{10} the heat transferred to the thermocouple. Heating
 225 the needle also induces transient variations in temperature within the whole
 226 system. Thermal properties of PEG can be obtained by considering the
 227 heat equation (conductive regime) in two domains assorted with boundary
 228 conditions. For this purpose, we use the quadrupole formalism proposed by
 229 Maillet *et al.* [29].

230 The first domain is bounded by the outer surface of the needle ($r_1 = r_e (\approx$
 231 $r_i)$) and a surface of the material sample ($r_2 \rightarrow \infty$). Following the method
 232 proposed by Maillet *et al.* [29], the thermal quadrupole formalism writes:

$$\begin{bmatrix} \theta_1 \\ \Phi_{12} \end{bmatrix} = [M1][M2] \begin{bmatrix} \theta_2 \\ \frac{\theta_2}{Z} \end{bmatrix} = \begin{bmatrix} 1 & 0 \\ C_1 p & 1 \end{bmatrix} \begin{bmatrix} 1 & R_1 \\ 0 & 1 \end{bmatrix} \begin{bmatrix} \theta_2 \\ \frac{\theta_2}{Z} \end{bmatrix} = \begin{bmatrix} 1 & R_1 \\ C_1 p & 1 + R_1 C_1 p \end{bmatrix} \begin{bmatrix} \theta_2 \\ \frac{\theta_2}{Z} \end{bmatrix} \quad (6)$$

with:

$\theta_1 = \mathcal{L}(T_1(t) - T_1(0))$ being the Laplace transform of the temperature varia-
 tion in the needle, i.e. $T_1(t) - T_1(0)$,

$\theta_2 = \mathcal{L}(T_2(t) - T_2(0))$ the Laplace transform of the temperature variation in
 the sample at the interface needle-material, i.e. $T_2(t) - T_2(0)$,

$\Phi_{12} = \mathcal{L}(\phi_{12})$ the Laplace transform of ϕ_{12} ,

$M1$ the quadrupolar matrix representing the needle as a pure capacity C_1 ,

$M2$ the quadrupolar matrix representing the contact resistance at the inter-
 face 1-2,

p the Laplace parameter (s^{-1}),

R_1 the thermal contact resistance per unit of length at the interface 1-2
 (m K W^{-1}), and

$$C_1 = \pi(r_e^2 - r_i^2)\rho_1 c_1, \quad (7)$$

$$Z = \frac{K_0(qr_e)}{2\pi\lambda q r_e K_1(qr_e)}, \quad (8)$$

$$q = \sqrt{\frac{p}{a}} \quad (9)$$

233 where ρ_1 is the density of the needle (kg m^{-3}), c_1 the specific heat of the
 234 needle ($\text{J K}^{-1} \text{kg}^{-1}$), a the thermal diffusivity of the sample ($\text{m}^2 \text{s}^{-1}$), and λ
 235 the thermal conductivity of the sample ($\text{W m}^{-1} \text{K}^{-1}$).

236 Similarly, we consider a second domain that is bounded by the thermocouple
 237 $r_0 = 0 (\approx r_t)$ and the inner needle surface $r_1 = r_i (\approx r_e)$. The quadrupole
 238 formalism leads to:

$$\begin{bmatrix} \theta_1 \\ \Phi_{10} \end{bmatrix} = [M3][M4] \begin{bmatrix} \theta_0 \\ 0 \end{bmatrix} = \begin{bmatrix} 1 & R_0 \\ 0 & 1 \end{bmatrix} \begin{bmatrix} 1 & 0 \\ C_0 p & 1 \end{bmatrix} \begin{bmatrix} \theta_0 \\ 0 \end{bmatrix} = \begin{bmatrix} 1 + R_0 C_0 p & R_0 \\ C_0 p & 1 \end{bmatrix} \begin{bmatrix} \theta_0 \\ 0 \end{bmatrix} \quad (10)$$

239 with:

240 $\theta_0 = \mathcal{L}(T_0(t) - T_0(0))$ being the Laplace transform of the thermocouple's
 241 temperature variation, i.e. $T_0(t) - T_0(0)$,

242 $\Phi_{10} = \mathcal{L}(\phi_{10})$ the Laplace transform of the heat flow rate ϕ_{10} ,

243 $M3$ the quadrupolar matrix representing the contact resistance at the inter-
 244 face 0-1,

245 $M4$ the quadrupolar matrix representing the thermocouple as a pure capac-
 246 ity C_0 ,

247 R_0 the thermal contact resistance per unit length between the thermocouple
 248 and the needle (m K W^{-1}), and

249

$$C_0 = \pi r_t^2 \rho_0 c_0, \quad (11)$$

250 where ρ_0 is the density of the thermocouple (kg m^{-3}) and c_0 the specific heat
 251 of the thermocouple ($\text{J K}^{-1} \text{kg}^{-1}$).

From Eq.(6) we deduce:

$$\theta_1 = \left(1 + \frac{R_1}{Z}\right) \theta_2, \quad (12)$$

$$\Phi_{12} = \left(C_1 p + \frac{1 + R_1 C_1 p}{Z}\right) \theta_2 = \left(C_1 p + \frac{1 + R_1 C_1 p}{Z}\right) \frac{\theta_1}{1 + \frac{R_1}{Z}}. \quad (13)$$

From Eq.(10) we deduce:

$$\theta_1 = (1 + R_0 C_0 p) \theta_0, \quad (14)$$

$$\Phi_{10} = C_0 p \theta_0 = \frac{C_0 p}{1 + R_0 C_0 p} \theta_1. \quad (15)$$

The Laplace transform of the total heat flow rate ϕ writes:

$$\mathcal{L}(\phi) = \frac{\phi}{p} = \Phi_{12} + \Phi_{10} = \left(\frac{Z C_1 p + 1 + R_1 C_1 p}{Z + R_1} + \frac{C_0 p}{1 + R_0 C_0 p}\right) \theta_1, \quad (16)$$

and by substituting Eq.(14) into Eq.(16) we obtain

$$\theta_0 = \frac{\phi}{p} \frac{Z + R_1}{(Z + R_1)[(C_0 + C_1)p + R_0 C_0 C_1 p^2] + 1 + R_0 C_0 p}. \quad (17)$$

At long time ($p \rightarrow 0$), the above equations simplify to:

$$\theta_0 = \frac{\phi}{p}(Z + R_1), \quad (18)$$

$$K_0(qr_e) = -\ln\left(\frac{qr_e}{2}\right) - \gamma, \quad (19)$$

$$K_1(qr_e) = \frac{1}{qr_e}, \quad (20)$$

$$\theta_0(p) = \frac{\phi}{p} \left[-\frac{\ln\left(\frac{qr_e}{2}\right)}{2\pi\lambda} - \frac{\gamma}{2\pi\lambda} + R_1 \right] = \quad (21)$$

$$= \frac{\phi}{p} \left[-\frac{\ln(p)}{4\pi\lambda} - \frac{\ln\left(\frac{r_e}{2\sqrt{a}}\right)}{2\pi\lambda} - \frac{\gamma}{2\pi\lambda} + R_1 \right]. \quad (22)$$

By performing the inverse Laplace transform, we obtain:

$$T_0(t) = \phi \left[\frac{\ln(t)}{4\pi\lambda} + \frac{\gamma}{4\pi\lambda} - \frac{\ln\left(\frac{r_e}{2\sqrt{a}}\right)}{2\pi\lambda} - \frac{\gamma}{2\pi\lambda} + R_1 \right], \quad (23)$$

and finally

$$T_0(t) = \frac{\phi}{4\pi\lambda} \ln(t) + \phi \left(\frac{-\gamma}{4\pi\lambda} - \frac{\ln\left(\frac{r_e}{2\sqrt{a}}\right)}{2\pi\lambda} + R_1 \right). \quad (24)$$

252 Equation (24) highlights a logarithm dependence of T_0 with time that
 253 becomes the dominant term at long time. This equation is valid only if the
 254 regime remains conductive and the medium is infinite. Hence, we can write:

$$T_0(t) = D_1 + D_2 \times \ln(t) \quad (25)$$

255 with D_1 and D_2 being two constants which depend on the material's thermal
 256 conductivity λ . Temperature measurements allow us to identify these two
 257 parameters by minimizing $S = \sum_{t_d}^{t_f} (T_{\text{exp}}(t) - T_0(t))^2$ on a time interval $[t_d, t_f]$,
 258 where T_{exp} is the experimental temperature measured by the thermocouple
 259 and T_0 the temperature obtained from Eq. (25). The thermal conductivity
 260 is finally obtained by evaluating the following equation:

$$\lambda = \frac{\phi}{4\pi D_2}. \quad (26)$$

261 At a given temperature, the experiments are repeated three times and the
 262 final value of conductivity is taken as the mean of these experiments. The
 263 maximum variation of λ obtained in this way is $0.02 \text{ W m}^{-1} \text{ K}^{-1}$.

264 *2.4. Specific heat capacity and latent heat*

265 The specific heat capacity c_p as well as the latent heat of the material are
 266 obtained using a Setaram μdSc3 differential calorimeter.

267 The protocol consists in applying temperature variations to the sample
 268 (sample mass about 200 - 300 mg) and in measuring simultaneously the
 269 heat transfer over time. Here, temperature variations are generated either
 270 through ramps of different rates of cooling/heating (1 K min^{-1} , 0.5 K min^{-1} ,
 271 0.2 K min^{-1}) or through temperature steps that lead to quasi-steady thermal
 272 conditions. In the latter case, steps last long enough to recover the steady
 273 state, that is, until there is no more heat flux between the sample and the
 274 device. In our experiments, this corresponds to a minimum of 1 hour up
 275 to 2 hours per temperature step. Increments between temperature steps are
 276 set to 1 K when phase change occurs, i.e. between 283.15 K and 303.15 K,
 277 to gain accuracy in evaluating the effective $c_p(T)$. Outside this temperature
 278 range, the increment is 2 K. The increment between two successive steps is
 279 obtained by applying a temperature ramp of 0.2 K min^{-1} .

280 Long steps or slow temperature variations have the advantage to avoid
 281 or at least to minimize undercooling effects [26]. Reversibility of results
 282 are tested performing the entire protocol both increasing and decreasing the
 283 temperature. The effective heat capacity is deduced from the heat transferred
 284 to the sample after each temperature variation. At the phase transition, the
 285 effective c_p varies strongly due to the addition of latent heat to sensible
 286 heat. The latent heat is therefore estimated by subtracting the sensible heat
 287 obtained for the liquid or solid phase from the total heat measured at the
 288 phase change.

289 A method validation for our experimental conditions and post-process is
290 provided in the supplementary materials.

291 **3. Results**

292 *3.1. Density*

293 *3.1.1. Liquid phase*

294 Density measurements of PEG 600 are presented in Fig. 5 in the tem-
295 perature range of [294.15, 373.15] K. Measurements have been performed by
296 cooling the sample in order to avoid any issues related with the formation of
297 bubbles (that occurs when the material is heated over a large temperature
298 range) or with the presence of a mushy phase at the beginning of the analysis,
299 i.e. around 294.15 K. This precaution enables to obtain reproducible density
300 values under our experimental conditions.

301 Our experimental values are summarized in Fig. 5 together with values
302 currently present in literature [18, 15, 16]. We observe a very good agreement
303 between our results and literature (see also Table 3 where deviations are
304 shown). Our results are found within a maximum difference of 1% from
305 those reported in the above cited studies. Our results can be fitted by a
306 linear model (continuous line in Fig. 5) as follows:

$$\rho(T) = p_1 \times T + p_2 \quad (\text{g cm}^{-3}), \quad (27)$$

307 with $p_1 = -0.00081643 \text{ g cm}^{-3} \text{ K}^{-1}$, $p_2 = 1.3652 \text{ g cm}^{-3}$ and T the tempera-
308 ture in K. The intervals of the coefficients with 95% confidence bounds are
309 $p_1 = [-0.0008182, -0.0008147]$ and $p_2 = [1.365, 1.366]$.

310 Furthermore, the thermal expansion coefficient β can be evaluated ac-
311 cording to Eq. (1). For instance, at $P = 1.007 \text{ bar}$ and $T_{ref} = 298.15 \text{ K}$, we
312 obtain $\rho_{ref} = 1.121961 \text{ g cm}^{-3}$ and $\beta = 7.28 \times 10^{-4} \text{ K}^{-1}$, with an estimated
313 standard uncertainty of $u(\beta) = 0.02 \times 10^{-4} \text{ K}^{-1}$.

314 *3.1.2. Solid phase*

315 The density of PEG 600 in solid phase is obtained using the pycnometer
316 described in section 2.2.2. A material sample of about 150 g is placed in the
317 upper cavity of the pycnometer. The latter is left inside the thermostatic
318 chamber for 24 hours at temperature of 273.75 K. This is done before per-
319 forming any measurement in order to ensure the complete solidification of the
320 sample. Density measurements are afterward carried out at the same tem-
321 perature of 273.75 K by keeping the pycnometer with the solid sample inside

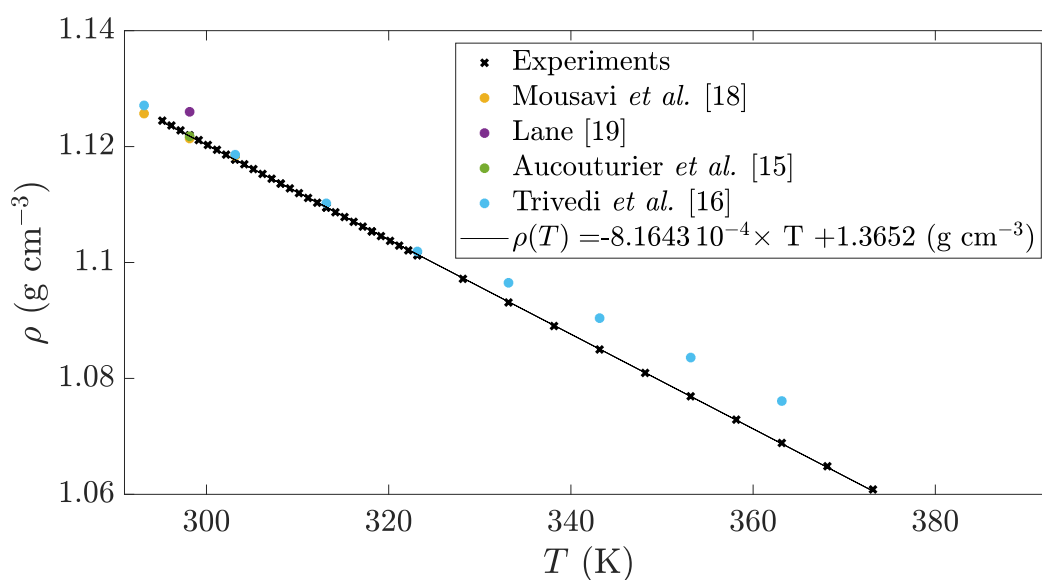


Figure 5: Density ρ of PEG 600 as a function of temperature T at the pressure $P=1.007$ bar. Data are provided in supporting files. Standard uncertainties u are $u(P)=0.018$ bar and $u(T) = 0.01$ K. The combined expanded uncertainty U_c is $U_c(\rho)=2\times 10^{-3}$ g cm $^{-3}$, with 0.95 level of confidence ($k=2$) and considering a contribution due to purity (x_e) of $u(x_e) = 0.002/\sqrt{3} = 0.0012$ after [18], who reported an initial purity of 99.8 % for samples of PEG 600 provided by the same manufacturer as ours.

Table 3: Comparison between some of our density measurements (ρ) of PEG 600 with values given in literature (ρ_{lit}) at different temperatures T and pressure $P=1.007$ bar^a.

T (K)	ρ (\times) (g cm^{-3})	ρ_{lit} (\circ) (g cm^{-3})	Reference	Deviation (%)
298.15	1.121961	1.126	[19]	0.36
		1.1214	[18]	0.05
		1.12177	[15]	0.02
303.15	1.117783	1.1184	[18]	0.06
		1.1186	[16]	0.07
313.15	1.109468	1.1102	[16]	0.07
323.15	1.101273	1.1019	[16]	0.06
333.15	1.093104	1.0965	[16]	0.31
343.15	1.084992	1.0904	[16]	0.50
353.15	1.076914	1.0836	[16]	0.62
363.15	1.068864	1.0761	[16]	0.67

Standard uncertainties u are $u(P)=0.018$ bar and $u(T) = 0.01$ K. The combined expanded uncertainty U_c is $U_c(\rho)=2\times 10^{-3}$ g cm^{-3} , with 0.95 level of confidence ($k=2$) and considering a contribution due to purity (x_e) of $u(x_e) = 0.002/\sqrt{3} = 0.0012$ after [18], who reported an initial purity of 99.8 % for samples of PEG 600 provided by the same manufacturer as ours.

Table 4: Pressure measurements performed for one sample of PEG 600 at 273.75 K. ^a

First set			Second set		
P_i (bar)	P_f (bar)	P_f/P_i	P_i (bar)	P_f (bar)	P_f/P_i
3.317	1.816	54.7 %	3.555	1.943	54.6 %
3.266	1.788	54.7 %	3.365	1.851	54.7 %
3.415	1.869	54.7 %	3.296	1.807	55.0 %
3.548	1.938	54.6 %	3.399	1.861	54.8 %

^aStandard uncertainties u are $u(P) = 0.001$ bar and $u(T) = 0.01$ K.

322 the thermostatic chamber for the entire duration of the experiment. Two
 323 sets of pressure measurements are performed, in each of which the measure-
 324 ment is repeated 4 times (see Table 4). After the first set of measurement,
 325 the sample is removed from the device and melted. The protocol is then
 326 performed again for the second set.

327 For the range of PEG volume involved in our experiments, the error of
 328 measurements is found smaller than 5%. This value is obtained using a
 329 stainless steel sample with a known volume of 3.92×10^{-5} m³. The volume
 330 measured with the pycnometer led to $V_{sample} = 3.82 \times 10^{-5}$ m³, i.e. within
 331 2.6 % difference with the real value.

332 The density of PEG 600 in solid phase and at 273.75 K is evaluated to
 333 $\rho = 1510$ kg m⁻³ with a standard uncertainty $u(\rho) = 23$ kg m⁻³. This value
 334 results to be quite different from the one obtained for the liquid phase. This
 335 is not surprising as it is correlated to the large variation in volume occurring
 336 during solidification.

337 3.2. Thermal conductivity

338 3.2.1. Liquid phase - Steady hot tube method

339 As above mentioned in section 2.3.1, the steady hot tube method is rel-
 340 evant only in the liquid phase as it requires good thermal contacts between
 341 sample and tubes surfaces. Since the device is filled with PEG 600 in liquid
 342 phase, the largest decrease in volume that leads to thermal resistances at
 343 interfaces is observed at the liquid-to-solid transition. At temperature below
 344 293.15 K results are indeed no longer reproducible. For higher temperatures,
 345 however, surface contact resistances can be assumed to be negligible. Mea-
 346 surements are performed at steady state. Results obtained with this device
 347 are presented in Fig. 6 ('+' symbols) as a function of the mean temperature

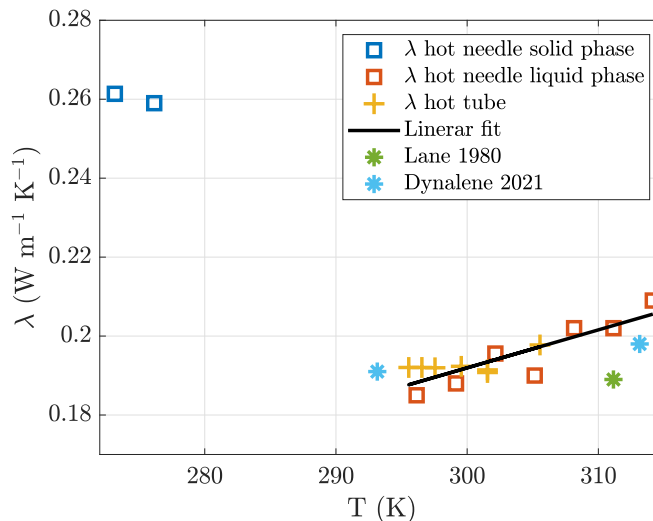


Figure 6: Thermal conductivity results for liquid phase and solid phases at the pressure $P=1.007$ bar. The temperature T refers (i) to the mean temperature between thermocouples $T = \bar{T} = (T_1 + T_2)/2$ in the case of the hot tube method and (ii) to the temperature in the thermostatic enclosure in the case of the hot needle method. Data are provided in supporting files. Standard uncertainties u are $u(P) = 0.018$ bar and $u(T) = 0.1$ K. The combined expanded uncertainty U_c is $U_c(\lambda) = 0.04$ W m⁻¹ K⁻¹ with 0.95 level of confidence ($k \approx 2$), for both hot tube method and hot needle method.

348 between the two thermocouples, i.e. $\bar{T} = T = (T_1 + T_2)/2$. For comparison,
 349 additional values of thermal conductivity given by Lane [19] and values from
 350 a data sheet provided by Dynalene [30] are also displayed in Fig. 6. In our
 351 experiments the temperature variation $\Delta T = T_2 - T_1$ does not exceed 3 K
 352 through the annular region of the device, i.e. between r_1 and r_2 . In the range
 353 of the tested temperatures, we observe a slight temperature dependence of
 354 λ . These measurements are complemented by those obtained by using the
 355 hot needle method.

356 3.2.2. Solid and liquid phases - Hot needle method

357 The measurements are carried out with the needle probe described pre-
 358 viously in Section 2.3.2. The estimation of the thermal conductivity λ is
 359 obtained assuming: (i) conductive regime in the vicinity of the needle, (ii)
 360 an infinite medium and (iii) $T_0(t) \propto \ln(t)$ at long time. The time interval
 361 $[t_i, t_f]$, in which the latter condition is satisfied, is determined empirically
 362 when the difference between experiments and the model is close to zero (see
 363 the discussion below about residuals).

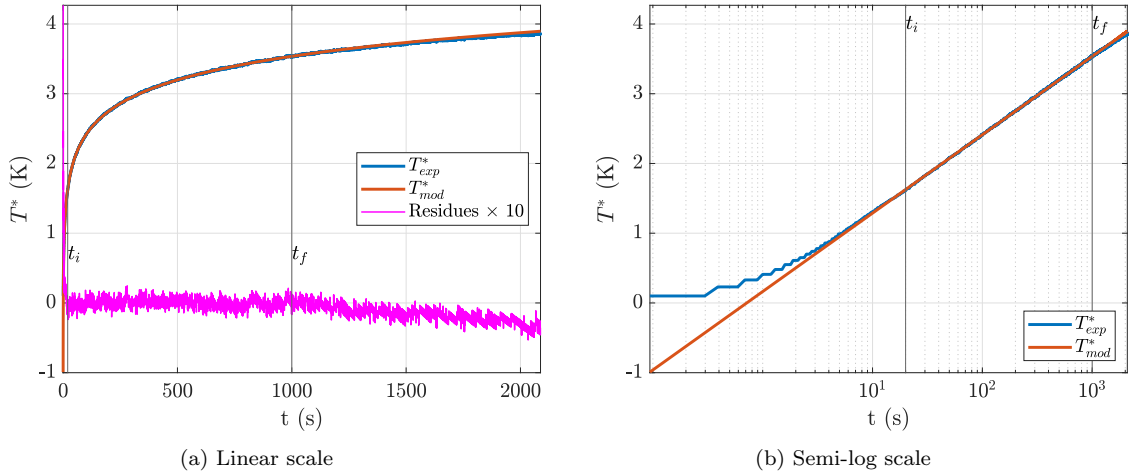


Figure 7: Time evolution of experimental (T_{exp}^* , in blue) and simulated (T_{mod}^* , in red) temperature difference T^* between the hot needle and the thermostatic enclosure set at 276.15 K and $P=1.007$ bar. The red curve is obtained with the simplified model from Eq. (25). Magenta curve in (a) displays the residues S between T_{exp} and T_{mod} multiplied by 10 times. Data are provided in supporting materials. Standard uncertainties u are $u(P)=0.018$ bar, $u(T^*)=0.02$ K and $u(t)=0.001$ s.

364 Thermal conductivity values in the solid phase are obtained placing the
 365 device in the temperature controlled binder. An example of temperature
 366 measurement ($T^* = T_0(t) - T_0(0)$) is plotted in Fig. 7 as a function of
 367 time. In the same figure we also display temperature values estimated by the
 368 model given by Eq. (25). Residuals multiplied by 10 times are also plotted in
 369 order to highlight the differences between measurements and the model. For
 370 each set of experiments, we determine the time interval $[t_i, t_f]$ along which
 371 residuals are perfectly flat and centered on zero, i.e. the time interval in
 372 which our model is consistent. This interval is bounded by vertical lines in
 373 Figs. 7 and 8. In the case presented in Fig. 7, the estimation time interval is
 374 $[20, 1000]$ s. The divergence of the residuals after 1000 s indicates the limit of
 375 validity of the infinite medium assumption. Following Eq. (25), we evaluate
 376 D_2 within the estimation interval as the slope of the temperature variation
 377 with time in semi-log scale (Fig. 7b).

378 The model also applies to the liquid phase only if convection does not
 379 occur. For this reason, we have also performed some measurements above
 380 293.15 K. We show them in Fig. 8, where experimental and simulated tem-
 381 perature variations are displayed as a function of time. The same conditions

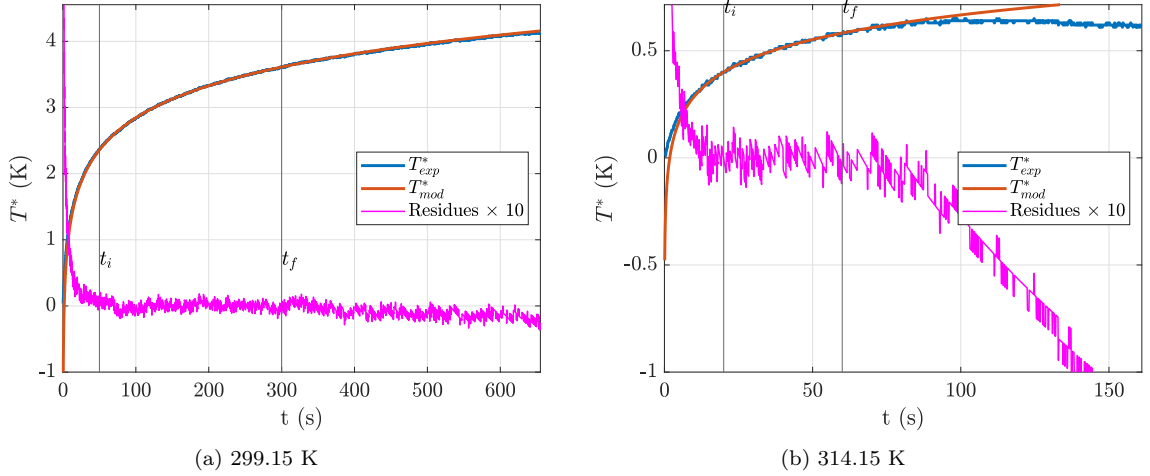


Figure 8: Time evolution of experimental (T_{exp}^* , in blue) and simulated (T_{mod}^* , in red) temperature difference T^* between the hot needle and the thermostatic enclosure set at $P=1.007$ bar and 299.15 K (a) and 314.15 K (b). The red curve is obtained with the simplified model from Eq. (25). Magenta curves display the residues between T_{exp}^* and T_{mod}^* multiplied by 10 times. Data are provided in supporting materials. Standard uncertainties u are $u(P)=0.018$ bar, $u(T^*)=0.02$ K and $u(t)=0.001$ s.

382 described above are assumed and residuals are again plotted multiplied by
 383 10 times. Figure 8 corresponds to two different temperatures imposed in the
 384 chamber, i.e. 299.15 K and 314.15 K. The estimation interval was adjusted
 385 to $[50, 300]$ s for the measurement at 299.15 K and to $[20, 60]$ s for the
 386 measurement at 314.15 K. The residuals are found flat and centered on zero
 387 over these intervals. In the case of 314.15 K, the divergence of the residuals
 388 after 60 s is explained by the occurrence of convection around the needle.
 389 The higher the temperature is, the earlier this phenomenon appears. For
 390 instance, convection is not observed before 300 s for the case at 299.15 K.

391 Figure 6 summarizes all the thermal conductivity measurements as a function of
 392 temperature carried out for PEG 600. In liquid phase, values obtained
 393 via the needle method (square symbols) are consistent with those obtained
 394 using the hot tube method. As temperature increases, the thermal conductivity
 395 in the liquid phase shows a slight increase. This follows a linear variation
 396 in the form of $\lambda(T) = 9.61 \times 10^{-4} T - 9.66 \times 10^{-2}$, with λ in $\text{W m}^{-1} \text{K}^{-1}$ and
 397 temperature T in K. The intervals of the coefficients with 95% confidence
 398 bounds are $p_1 = [0.0006076, 0.001316]$ and $p_2 = [-0.2037, 0.01055]$.

399 Our results are very close to those provided by Dynalene (see the data

400 sheet in [30]), i.e. $\lambda = 0.191 \text{ W m}^{-1} \text{ K}^{-1}$ at 293.15 K and $\lambda = 0.198$
 401 $\text{W m}^{-1} \text{ K}^{-1}$ at 313.15 K. A good agreement is also found with values pub-
 402 lished by Lane [19], who obtained $\lambda = 0.189 \text{ W m}^{-1} \text{ K}^{-1}$ at 311.00 K and
 403 $\lambda = 0.187 \text{ W m}^{-1} \text{ K}^{-1}$ at 340.15 K.

404 In solid phase, the value of conductivity measured at 273.15 K and 276.15
 405 K does not vary much, leading for this temperature interval to $\lambda_s \approx 0.260$
 406 $\text{W m}^{-1} \text{ K}^{-1}$, with a standard uncertainty of $u(\lambda)=0.02 \text{ W m}^{-1} \text{ K}^{-1}$. This
 407 value is close to the one proposed by Kou et al [14] for PEG 1000, i.e.
 408 $0.29 \pm 0.05 \text{ W m}^{-1} \text{ K}^{-1}$. In our experiments, for an enclosure temperature
 409 of 279.15 K, the temperature near the needle is around 283.00 K and the
 410 material starts to melt. This makes it difficult to obtain values of λ of PEG
 411 600 in solid phase above 276.15 K. The gap between 276.15 K and 293.15 K
 412 in terms of thermal conductivity (Fig. 6) is explained by the occurrence of
 413 the phase transition.

414 To summarize, our measurements provide values of thermal conductivity
 415 in both liquid and solid phases. An effective value of λ in solid phase can
 416 be measured in the temperature range [276.15, 293.15] K. However, we think
 417 that a careful investigation of the material structure at the phase transition
 418 would be more relevant. This aspect is beyond the scope of this article but
 419 it will be investigated in the near future.

420 3.3. Specific heat capacity and latent heat

421 Raw data obtained by differential scanning calorimetry are presented in
 422 Fig. 9. The figure displays the amount of heat flux (in blue) transferred
 423 between the PCM sample and the calorimeter, for the case of imposed tem-
 424 perature steps (in red). Each increment of temperature leads to a peak in
 425 terms of heat exchanged. The latter goes back to zero as soon as the thermal
 426 equilibrium is reached. Given this experimental protocol, the effective heat
 427 capacity c_p is deduced by integrating the heat flux over the duration of a step
 428 (including the increment) and dividing the result by the mass of the sample
 429 m and the temperature increment.

430 On the other hand, when the protocol involves temperature ramps, i.e.
 431 continuous temperature variations with time, we directly determine the ef-
 432 fective c_p from the measured heat flux ϕ according to

$$\phi = mc_p \frac{dT}{dt}, \quad (28)$$

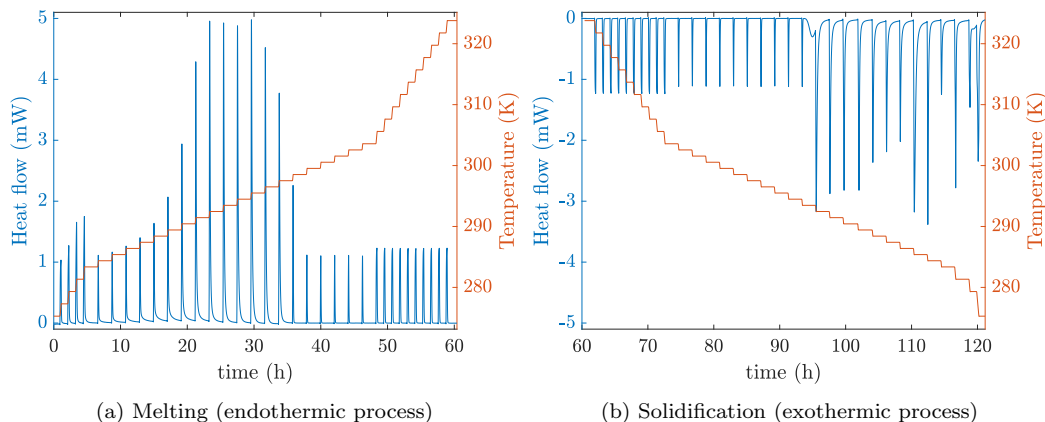


Figure 9: Heat flow rate measured from DSC (in blue) and imposed temperature steps (in red) as a function of time and at the pressure $P=1.007$ bar. (a) Melting of PEG 600 for increasing temperature steps (endothermic process). (b) Solidification of PEG 600 for decreasing temperature steps (exothermic process). Data are provided in supporting files. Standard uncertainties u are $u(P)=0.018$ bar, $u(\text{Heat flow})=0.01$ mW and $u(T)=0.01$ K.

433 where the temperature variation rate $\frac{dT}{dt}$ is constant and imposed by the
 434 ramp. We deduce then:

$$c_p = \frac{\phi}{m} \left(\frac{dT}{dt} \right)^{-1}. \quad (29)$$

435 The resulting values of effective c_p are shown in Fig. 10 as a function
 436 of temperature. Similar trends are observed for all tested protocols. When
 437 the material is liquid, i.e. for large temperature values (above 298.15 K) and
 438 at pressure $P=1.007 \pm 0.018$ bar, we obtain a quasi constant heat capacity,
 439 i.e. $c_p = 2.13$ kJ kg⁻¹ K⁻¹, corresponding to 1278 J K⁻¹ mol⁻¹. The standard
 440 uncertainty for c_p is 0.06 kJ kg⁻¹ K⁻¹. This value of heat capacity is recovered
 441 in the liquid phase for both cooling and heating experiments. However, as
 442 shown in Fig. 10, we do not obtain a constant value of c_p around 280 K,
 443 i.e. a temperature close to but below the solidification/melting peaks. The
 444 values are provided in the supplementary material. Similar tendencies are
 445 observed in [14].

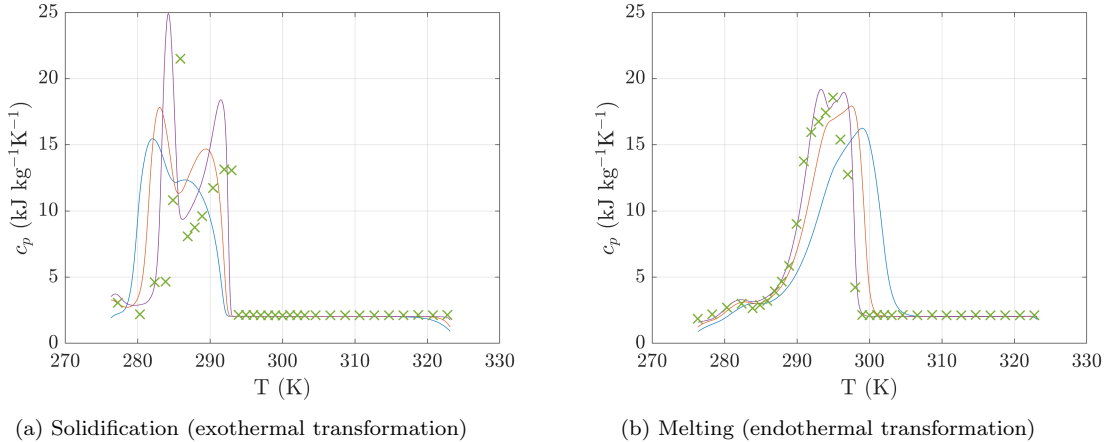
446 In the temperature range where the phase transition occurs (i.e. solidifi-
 447 cation in Fig. 10a and melting in Fig. 10b), variations in the evaluated c_p
 448 are due to the competition between the kinetics of the phase change process

449 and the rate of temperature variations. This competition leads to a tempera-
450 ture hysteresis during solidification that corresponds to undercooling effects.
451 This latter phenomena decreases for slow temperature variations. In the case
452 of imposed temperature steps, the melting of PEG 600 is observed between
453 283.4 K and 298.5 K, while its solidification occurs between 294.5 K and
454 281.3 K. Further differences between melting and freezing processes can be
455 highlighted. Indeed, two distinct local maxima are observed during solidifi-
456 cation as the temperature decreases (Fig. 10a). These extrema are always
457 obtained for similar temperature values when the adopted cooling protocol
458 lasts long enough. Here, extrema correspond to exothermal transformations
459 correlated to structural modifications that occur during the crystallization
460 [20, 21].

461 Reciprocally, at least one extremum value in terms of c_p is also obtained
462 for the melting process (Fig. 10b). When the heating process is long enough
463 (0.2 K min^{-1}), two local peaks are observed but their amplitudes are smaller
464 than in the case of the solidification process. These multiple peaks are ob-
465 served also in other studies where they are attributed to microstructural
466 variations, i.e. crystals with different thickness due to variations in folds
467 number in the polymer chain [31] or due to the evolution of the lamellar
468 microstructure during the phase change [32].

469 A comparison of the effective c_p obtained for PEG 600 with PEGs with
470 higher molar masses [14] is proposed in Fig. 11. All results are obtained
471 during the melting process and by heating samples with a rate of 1 K min^{-1}
472 for PEG 600 and a rate of 10 K min^{-1} [14] for PEG with large molar masses
473 (from 1000 to 20000). Our data for PEG 600 follow similar tendencies to
474 those observed by [14] as the average molar mass of PEG increases, i.e. both
475 melting temperature and c_p increase.

476 Finally, the latent heat is evaluated by integrating only the part due to the
477 phase transition in the effective heat capacity. For the solidification process,
478 the integration leads to a latent heat of 128.0 kJ kg^{-1} , while for the melting
479 to 128.7 kJ kg^{-1} . In both cases, we estimate a standard uncertainty for the
480 latent heat of 2 kJ kg^{-1} . These values are in very good agreement with the
481 one proposed by Lane [19], i.e. 127.2 kJ kg^{-1} . According to Pielichowski
482 & Flejtuch [33], the latent heat of melting of a 100% crystalline polymer is
483 196.8 kJ kg^{-1} . Compared with this latter value, PEG 600 should correspond
484 to a degree of crystallinity of 65%. Indeed, low molecular weight polymers
485 are known to have higher segmental mobility, thus reducing the formation of
486 the crystalline phase (geometric alignment), as observed for PEG at different



(a) Solidification (exothermal transformation)

(b) Melting (endothermal transformation)

Figure 10: Effective $c_p(T)$ evaluated at constant pressure $P=1.007$ bar and during (a) the solidification process and (b) the melting process, for temperature variations of 1 K min^{-1} (blue lines), 0.5 K min^{-1} (red lines), 0.2 K min^{-1} (purple lines) and temperature steps (green crosses). Data are provided in supporting materials. Standard uncertainties u are $u(P)=0.018$ bar, $u(\text{Heat flow})=0.01$ mW, $u(T)=0.01$ K, $u(m)=0.01$ mg and $u(c_p)=0.06 \text{ kJ kg}^{-1} \text{ K}^{-1}$.

487 molecular weight [14, 33].

488 4. Conclusion

489 In this study we report the thermal properties of polyethylene glycol 600
 490 (PEG 600). The density in liquid phase has been measured in the tempera-
 491 ture range [298.15, 373.15] K. Given the small temperature increments used,
 492 we have been able to provide a fit for the temperature-dependent density of
 493 liquid PEG 600. The latter allows to determine the coefficient of thermal vol-
 494 ume expansion with a good accuracy. The density of PEG 600 in solid phase
 495 has been measured by using a pycnometer and it results in $\rho = 1510 \text{ kg m}^{-3}$
 496 with a standard uncertainty $u(\rho) = 23 \text{ kg m}^{-3}$ at 273.75 K. The variation
 497 of density between the two phases highlights a quite large volume shrinkage
 498 of the material during solidification. This can have a drastic consequence on
 499 thermal contacts at interfaces and hence a strong impact in the usability of
 500 this PCM in thermal energy storage systems.

501 The thermal conductivity λ has been investigated with two different meth-
 502 ods. Results for the liquid phase show a slight linear increase of λ with in-
 503 creasing temperature. For the solid phase, and within the investigated tem-

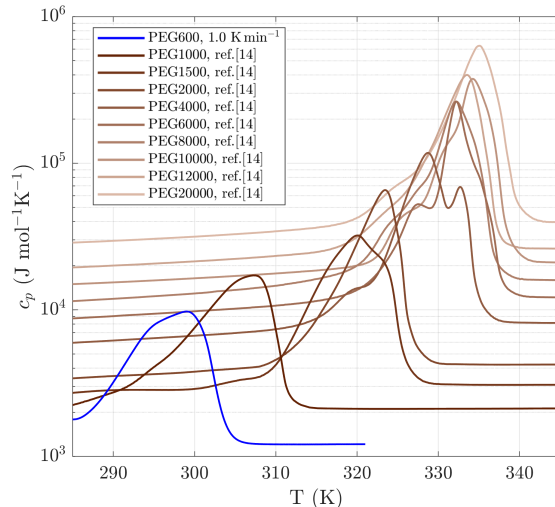


Figure 11: Comparison between the effective $c_p(T)$ for PEG 600 (blue line) and data of [14] for PEG with large molar masses (brown lines). In both cases, the curves are obtained from DSC measurements during the melting process. For a better comparison, heat capacity is plotted in $\text{J mol}^{-1} \text{K}^{-1}$. For PEG 600 we display the same curve shown in Fig. 10b for a heating rate of 1.0 K min^{-1} . Uncertainties are those reported in Fig. 10b.

504 perature range, we find $\lambda \approx 0.260 \text{ W m}^{-1} \text{K}^{-1}$ with a standard uncertainty
 505 of $u(\lambda)=0.02 \text{ W m}^{-1} \text{K}^{-1}$.

506 Effective heat capacity and heat transfer have been described and quan-
 507 tified by DSC measurements. Far from the phase transition, we obtain a
 508 constant specific heat capacity for both solid and liquid phase. Whether
 509 the sample is slowly cooled or heated, the phase transition starts at 283.4 K
 510 and at 294.5 K for the melting and solidification process, respectively. Under-
 511 cooling effects are responsible for the hysteresis in phase change temperature,
 512 however they decrease when the cooling rate is decreased. DSC experiments
 513 enable us to obtain a latent heat of about 128.0 kJ kg^{-1} , which is close to the
 514 value proposed by Lane [19]. Furthermore, during the solidification process
 515 we observe several exothermic heat flow peaks that highlight consecutive re-
 516 organizations of aggregates and/or crystals in the internal structure of PEG
 517 600. This latter aspect is beyond the scope of this study. However, since
 518 explanations on PEG crystallization are still controversial in literature, a
 519 proper investigation at small scales of this process will be a fundamental
 520 part of our future work.

521 **Appendix A. Estimation of the error due to steady-state contact**
 522 **resistances**

523 During solidification, the density of the sample increases and $\rho_l < \rho_s$, with
 524 ρ_l being the density of the liquid phase and ρ_s the one of the solid phase.
 525 This results in a decrease in volume with temperature. In the hot tube device
 526 used to measure the thermal conductivity, this leads to an air/vacuum layer
 527 of thickness ϵ between the sample and the inner heating tube of radius r_1
 528 (Fig. 2).

529 One can write:

$$\rho_l \pi (r_2^2 - r_1^2) = \rho_s \pi [r_2^2 - (r_1 + \epsilon)^2], \quad (\text{A.1})$$

leading to

$$\epsilon = \left[r_2^2 - \frac{\rho_l}{\rho_s} (r_2^2 - r_1^2) \right]^{0.5} - r_1.$$

530 The thermal resistance between the two tubes is:

$$R = \frac{1}{2\pi\lambda} \ln \left(\frac{r_2}{r_2 - r_1 - \epsilon} \right) + \frac{1}{2\pi\lambda_{air}} \ln \left(\frac{r_1 + \epsilon}{r_1} \right) = \frac{1}{2\pi\lambda_m} \ln \left(\frac{r_2}{r_1} \right). \quad (\text{A.2})$$

531 In this way, λ_m is the measured value of the thermal conductivity while
 532 λ is the real thermal conductivity of the solid sample. We deduce:

$$\lambda_m = \ln \left(\frac{r_2}{r_1} \right) \left[\frac{1}{\lambda} \ln \left(\frac{r_2}{r_2 - r_1 - \epsilon} \right) + \frac{1}{\lambda_{air}} \ln \left(\frac{r_1 + \epsilon}{r_1} \right) \right]^{-1}. \quad (\text{A.3})$$

533 The radii values are $r_1 = 2.75$ mm; $r_2 = 6$ mm. With an estimated
 534 value for the thermal conductivity in solid phase of $\lambda = 0.26$ W m⁻¹ K⁻¹, we
 535 can calculate the value λ_m that we would have measured with the hot tube
 536 method. For $\rho_l/\rho_s = 0.75$, the calculation leads to $\lambda_m = 0.19$ W m⁻¹ K⁻¹, i.e.
 537 around 30% less than the actual value. For this reason, the steady-state hot
 538 tube device used in this study to measure λ of liquid PEG 600 is unsuitable
 539 to retrieve λ of the solid phase. For measurements of thermal conductivity
 540 of solid PCMs is therefore preferable to use a transient measurement device
 541 where contact resistances have no influence on estimating the conductivity.

542 **Acknowledgments**

543 Financial supports have been brought to this work by the operation
544 “STOCK’NRJ” co-financed by the European Union within the framework
545 of the Program FEDER-FSE Lorraine and Massif des Vosges 2014-2020.
546 This work is part of the ”CONVINCES” project financially supported by
547 the French National Research Agency (ANR).

548 **References**

- 549 [1] M. Kobayashi, T. Koide, S.-H. Hyon, Tribological characteristics of
550 polyethylene glycol (PEG) as a lubricant for wear resistance of ultra-
551 high-molecular-weight polyethylene (UHMWPE) in artificial knee joint,
552 Journal of the Mechanical Behavior of Biomedical Materials 38 (2014)
553 33–38.
- 554 [2] K. Bjugstad, D. Redmond Jr, K. Lampe, D. Kern, J. Sladek Jr, M. Ma-
555 honey, Biocompatibility of PEG-based hydrogels in primate brain, Cell
556 Transplantation 17 (4) (2008) 409–415.
- 557 [3] A. K. Jain, A. K. Goyal, N. Mishra, B. Vaidya, S. Mangal, S. P. Vyas,
558 PEG–PLA–PEG block copolymeric nanoparticles for oral immunization
559 against hepatitis B, International Journal of Pharmaceutics 387 (1-2)
560 (2010) 253–262.
- 561 [4] S. M. Baygi, S. Sadrameli, Thermal management of photovoltaic so-
562 lar cells using polyethylene glycol 1000 (PEG1000) as a phase change
563 material, Thermal Science and Engineering Progress 5 (2018) 405–411.
- 564 [5] F. Hamad, E. Egelle, K. Cummings, P. Russell, Investigation of the
565 melting process of polyethylene glycol 1500 (PEG 1500) in a rectangular
566 enclosure, International Journal of Heat and Mass Transfer 114 (2017)
567 1234–1247.
- 568 [6] J. Wang, M. Yang, Y. Lu, Z. Jin, L. Tan, H. Gao, S. Fan, W. Dong,
569 G. Wang, Surface functionalization engineering driven crystallization
570 behavior of polyethylene glycol confined in mesoporous silica for shape-
571 stabilized phase change materials, Nano Energy 19 (2016) 78–87.

- 572 [7] J. Yang, E. Zhang, X. Li, Y. Zhang, J. Qu, Z.-Z. Yu, Cellulose/graphene
573 aerogel supported phase change composites with high thermal conduc-
574 tivity and good shape stability for thermal energy storage, *Carbon* 98
575 (2016) 50–57.
- 576 [8] J. Jin, F. Lin, R. Liu, T. Xiao, J. Zheng, G. Qian, H. Liu, P. Wen,
577 Preparation and thermal properties of mineral-supported polyethylene
578 glycol as form-stable composite phase change materials (CPCMs) used
579 in asphalt pavements, *Scientific Reports* 7 (1) (2017) 1–10.
- 580 [9] Y. Zhou, X. Liu, D. Sheng, C. Lin, F. Ji, L. Dong, S. Xu, H. Wu,
581 Y. Yang, Graphene oxide/polyurethane-based solid–solid phase change
582 materials with enhanced mechanical properties, *Thermochimica Acta*
583 658 (2017) 38–46.
- 584 [10] A. Sharma, V. V. Tyagi, C. Chen, D. Buddhi, Review on thermal energy
585 storage with phase change materials and applications, *Renewable and*
586 *Sustainable Energy Reviews* 13 (2) (2009) 318–345.
- 587 [11] B. Zalba, J. M. Marin, L. F. Cabeza, H. Mehling, Review on thermal
588 energy storage with phase change: materials, heat transfer analysis and
589 applications, *Applied Thermal Engineering* 23 (3) (2003) 251–283.
- 590 [12] M. Firoozzadeh, A. H. Shiravi, M. Shafiee, Experimental and ana-
591 lytical study on enhancing efficiency of the photovoltaic panels us-
592 ing Polyethylene-Glycol 600 (PEG 600) as a phase change mate-
593 rial, *Iranian Journal of Energy and Environment* 10 (2019) 23–32.
594 doi:10.5829/ijee.2019.10.01.04.
- 595 [13] R. Velraj, R. Seeniraj, B. Hafner, C. Faber, K. Schwarzer, Heat transfer
596 enhancement in a latent heat storage system, *Solar Energy* 65 (3) (1999)
597 171–180.
- 598 [14] Y. Kou, S. Wang, J. Luo, K. Sun, J. Zhang, Z. Tan, Q. Shi, Thermal
599 analysis and heat capacity study of polyethylene glycol (PEG) phase
600 change materials for thermal energy storage applications, *The Journal*
601 *of Chemical Thermodynamics* 128 (2019) 259–274.
- 602 [15] C. Aucouturier, G. Roux-Desgranges, A. Roux, Excess molar volumes
603 and excess molar heat capacities of (polyethylene glycols+ water) at

- 604 temperatures between $T=278$ K and $T=328$ K, The Journal of Chemical
605 Thermodynamics 31 (2) (1999) 289–300.
- 606 [16] S. Trivedi, C. Bhanot, S. Pandey, Densities of poly(ethylene glycol)+
607 water over the temperature range (283.15 to 363.15) K, The Journal of
608 Chemical Thermodynamics 42 (11) (2010) 1367–1371.
- 609 [17] A. Singh, R. Walvekar, M. Khalid, W. Y. Wong, T. Gupta, Thermo-
610 physical properties of glycerol and polyethylene glycol (PEG 600) based
611 DES, Journal of Molecular Liquids 252 (2018) 439–444.
- 612 [18] Z. Mousavi, M. Pirdashti, A. A. Rostami, E.-N. Dragoi, Thermophysical
613 properties analysis of poly (ethylene glycol) 600+ methanol, ethanol, 1-
614 propanol, and 2-propanol binary liquid mixtures, International Journal
615 of Thermophysics 41 (2) (2020) 1–26.
- 616 [19] G. A. Lane, Low temperature heat storage with phase change materials,
617 International Journal of Ambient Energy 1 (3) (1980) 155–168.
- 618 [20] L. Yang, T. Smith, Melting and solidification behavior of blends of high
619 density polyethylene with poly (butylene terephthalate), Polymer Engi-
620 neering & Science 33 (21) (1993) 1426–1430.
- 621 [21] A. Azri, P. Giamarchi, Y. Grohens, R. Olier, M. Privat, Polyethylene
622 glycol aggregates in water formed through hydrophobic helical struc-
623 tures, Journal of Colloid and Interface Science 379 (1) (2012) 14–19.
- 624 [22] B. Bogdanov, A. Vidts, E. Schacht, H. Berghmans, Isothermal crys-
625 tallization of poly (ϵ -caprolactone- ethylene glycol) block copolymers,
626 Macromolecules 32 (3) (1999) 726–731.
- 627 [23] K. Pielichowski, K. Flejtuch, Differential scanning calorimetry studies
628 on poly (ethylene glycol) with different molecular weights for thermal
629 energy storage materials, Polymers for Advanced Technologies 13 (10-
630 12) (2002) 690–696.
- 631 [24] D. D. Gray, A. Giorgini, The validity of the Boussinesq approximation
632 for liquids and gases, International Journal of Heat and Mass Transfer
633 19 (5) (1976) 545–551.

- 634 [25] Y. Jannot, A. Degiovanni, Thermal properties measurement of materi-
635 als, John Wiley & Sons, 2018.
- 636 [26] N. R. Sgreva, J. Noel, C. Metivier, P. Marchal, H. Chaynes, M. Isaiev,
637 Y. Jannot, Thermo-physical characterization of hexadecane during the
638 solid/liquid phase change, *Thermochimica Acta* (2022) 179 – 180.
- 639 [27] J. Huetz, J.-P. Petit, Notions de transfert thermique par convection,
640 *Techniques de l'Ingénieur* (A1504A) (Aug. 1990).
- 641 [28] M. L. V. Ramires, C. A. Nieto de Castro, Y. Nagasaka, A. Nagashima,
642 M. J. Assael, W. A. Wakeham, Standard reference data for the thermal
643 conductivity of water (1994).
- 644 [29] D. Maillet, S. Andre, J. C. Batsale, A. Degiovanni, C. Moyne, Ther-
645 mal quadrupoles: solving the heat equation through integral transforms,
646 Wiley-Blackwell, 2000.
- 647 [30] Dynalene Inc., PEG Series: Techincal data sheet,
648 [https://www.dynalene.com/product-category/heat-transfer-](https://www.dynalene.com/product-category/heat-transfer-fluids/polyethylene-glycol-heat-transfer-fluids/)
649 [fluids/polyethylene-glycol-heat-transfer-fluids/](https://www.dynalene.com/product-category/heat-transfer-fluids/polyethylene-glycol-heat-transfer-fluids/).
- 650 [31] B. Wunderlich, *Macromolecular physics: Crystal nucleation, Growth,*
651 *Annealing 2* (1976).
- 652 [32] M. S. Lisowski, Q. Liu, J. Cho, J. Runt, F. Yeh, B. S. Hsiao, Crystalliza-
653 tion behavior of poly (ethylene oxide) and its blends using time-resolved
654 wide-and small-angle X-ray scattering, *Macromolecules* 33 (13) (2000)
655 4842–4849.
- 656 [33] K. Pielichowski, K. Flejtuch, Differential scanning calorimetry studies
657 on poly (ethylene glycol) with different molecular weights for thermal
658 energy storage materials, *Polymers for Advanced Technologies* 13 (10-
659 12) (2002) 690–696.